# Fibrous silica mesoporous ZSM-5 for carbon monoxide methanation

L.P. Teh[a], S. Triwahyono[a,b,*], A.A. Jalil[c,d], M.L. Firmansyah[a], C.R. Mamat[a], Z.A. Majid[a]

[a] Department of Chemistry, Faculty of Science, Universiti Teknologi Malaysia UTM, 81310 Johor Bahru, Johor, Malaysia
[b] Centre for Sustainable Nanomaterials, Ibnu Sina Institute for Scientific and Industrial Research, Universiti Teknologi Malaysia UTM, 81310 Johor Bahru, Johor, Malaysia
[c] Centre of Hydrogen Energy, Institute of Future Energy, Universiti Teknologi Malaysia UTM, 81310 Johor Bahru, Johor, Malaysia
[d] Department of Chemical Engineering, Faculty of Chemical and Energy Engineering, Universiti Teknologi Malaysia, 81310 UTM Johor Bahru, Johor, Malaysia

## ABSTRACT

A core-shell fibrous silica mesoporous ZSM-5 (FmZSM-5) has been developed by employing microemulsion system coupled with zeolite crystal-seed crystallization method and unprecedented applied in CO methanation. The FmZSM-5 showed greatly enhanced catalytic activity with the rate of CO conversion (0.0708 $\mu$mol-CO/m$^2$ s) and the rate of CH$_4$ formation (0.0488 $\mu$mol-CH$_4$/m$^2$ s) at 723 K, which is two-fold higher than that of the conventional recrystallized mZSM-5 (RmZSM-5). Besides, it showed high stability with no sign of deactivation up to 50 h. The presence of oxygen vacancies led to the increase in interparticle porosity, basicity, and CO and H$_2$ adsorption sites which are believed to be the keys for remarkably improved in CO methanation. Additionally, the influence of diffusion limitation was indicated to be negligible. Such a unique core-shell fibrous silica mesoporous ZSM-5 and their excellent catalytic properties suggest the significant application possibilities in base-catalyzed reaction especially in the production of methane.

© 2016 Elsevier B.V. All rights reserved.

## 1. Introduction

Conversion of syngas (CO + H$_2$) to synthetic natural gas (SNG), which mainly composed of methane, is widely explored due to the desire for the alternative energy source [1–3] and protecting the environment by recycling carbon sources (CO and/or CO$_2$) effectively based on the catalytic methanation [4]. The methanation of CO is not only an indispensable way in the production of methane, but also a purification method to avoid residual CO for poisoning the H$_2$-rich gas fuel cells [5,6]. Therefore, great efforts are made in the development of efficient catalysts for CO methanation.

Despite the extensive amount of the available literature regarding this topic, there are almost no reports about the effect of oxygen vacancies in surface defect of fibrous silica mesoporous ZSM-5 on the catalytic performance of CO methanation. The surface defect of support material represents the crucial nature in order to determine their properties–catalytic activity relationship towards CO methanation as the surface accessibility could become an issue limiting the applications in certain cases. Therefore, the nature of

surface defect is a topical issue and a real challenge for the heterogeneous catalytic reactions.

The microemulsion system was first proposed by Schulman et al. [7]. Microemulsion solution usually containing four components, namely a polar phase (usually water), a nonpolar phase (usually an aliphatic or aromatic hydrocarbon), a surfactant, and co-surfactant (generally 4–8 carbon chain aliphatic alcohol). The microemulsion is a reliable approach for controlling synthesis of the particle properties such as mechanisms of particle size control, geometry, morphology, homogeneity and surface area [8].

The microemulsion synthesis route is promising for controlling the morphology of a variety of zeolites and molecular sieves. Generally, zeolites are very versatile support materials that can be tailored to achieve optimum performance in a wide range of catalytic reactions. Therefore, zeolite catalysts are of great interest for purely fundamental reasons because they can be tailored to allow careful and systematic studies of various properties–activity relationships [9]. Lin et al. altered the morphology of silicalite-1 zeolite from coffin-shaped to novel rod-shaped and to irregular-shaped by varying the microemulsion composition [10]. On the contrary, Lee et al. synthesized spherical and platelet-shaped silicalite-1 zeolite by using the nonionic microemulsion technique. They suggested that the current technique can be applied to the synthesis of complex zeolitic materials with unique morphological properties and hierarchical structure [11].

* Corresponding author at: Department of Chemistry, Faculty of Science, Universiti Teknologi Malaysia UTM, 81310 Johor Bahru, Johor, Malaysia.
*E-mail address:* sugeng@utm.my (S. Triwahyono).

On the basis of the limited literature in this area, our effort has been focused on preparing a core-shell fibrous silica mesoporous ZSM-5 for enhanced activity in CO methanation. The material was prepared via a microemulsion system coupled with zeolite crystal-seed crystallization method. In the present study, the significance role of the oxygen vacancy effect on the physicochemical properties and its relationship to the catalytic performance of CO methanation was investigated and discussed. The highly accessible fibrous morphology of the material exhibited excellent catalytic performance than those of the conventional coffin morphology. Undeniably, the combination of unique core-shell structure and physicochemical properties such as oxygen vacancies that contributed to the high interparticle porosity, high basicity, and high CO and $H_2$ adsorption sites are responsible for the greatly enhanced catalytic performance and high stability in CO methanation. Besides, the accessibility of active sites was evaluated by the means of Mears' and Weisz-Prater criteria.

## 2. Experimental

### 2.1. Catalyst preparation

A core-shell fibrous silica mesoporous ZSM-5 (FmZSM-5) was prepared by microemulsion system coupled with zeolite crystal-seed crystallization method. Mesoporous ZSM-5 (mZSM-5) was used as the seed for this crystal-seed crystallization, prepared according to the previously reported procedure [12]. In brief, mesoporous ZSM-5 was prepared by the dual templating method using tetrapropylammonium bromide (TPA-Br) as a micropore-directing agent and benzalkonium chloride as a mesopore-directing agent. The starting parameters are Si/Al = 22.90, $H_2O$/Si = 18.30, TPA-Br/Si = 0.17, benzalkonium chloride/Si = 0.06, and NaOH/Si = 0.15. Firstly, the mixture of TPA-Br, benzalkonium chloride, sodium hydroxide (NaOH), and distilled water ($H_2O$) was homogeneously mixed under vigorous stirring for 5 min at room temperature. Then, aluminium hydroxide, $Al(OH)_3$ and tetraethyl orthosilicate (TEOS), $Si(OC_2H_5)_4$ were added to the mixture. The mixture was vigorously stirred for another 3 h at room temperature. After that, it was transferred into the autoclave and maintained at 423 K for 0.5 days. The as-synthesized sample was then washed and filtered, followed by dried at 383 K for 3 h and calcined at 823 K for 3 h. The prepared catalyst was denoted as mZSM-5. For preparation of FmZSM-5, TEOS was firstly dissolved in a mixture of toluene and 1-butanol. After that, mZSM-5 seed was added to the solution and stirred for 30 min. Then, a mixed solution of cetyltrimethylammonium bromide (CTAB), urea and distilled water was added and stirred to obtain a homogeneous solution. The resulting solution was exposed to microwave radiation (400 W) for 4 h. The solid product was isolated by centrifugation at 4000 rpm, followed by washing with acetone and distilled water, and then drying overnight in air at 383 K. Lastly, the solid product was calcined at 823 K for 6 h. The synthesis parameters were $H_2O$/Si = 165.34, CTAB/Si = 0.99, toluene/Si = 28.00, and 1-butanol/Si = 1.63. With the absence of TEOS, a recrystallized mZSM-5 (RmZSM-5) was also prepared by the same method. The metal analysis of RmZSM-5 and FmZSM-5 was determined by Agilent 4100 MP-AES spectrometer. The result showed that no other metal presents in the samples beside silicon and aluminium.

### 2.2. Catalyst characterization

The crystallinity of the catalysts were confirmed by X-ray diffraction (XRD) recorded on a Bruker Advance D8 X-ray powder diffractometer using Cu Kα radiation source (40 kV, 40 mA) at a 2θ angle ranging from 2° to 40° with a scan rate of 0.1° continuously.

The morphological properties of the catalysts were performed using FESEM-EDX (JEOL JSM-6701F) and TEM (Philips EM420).

The local environments of Al and Si atoms were analyzed using $^{27}Al$ and $^{29}Si$ solid-state magic-angle spinning (MAS) nuclear magnetic resonance (NMR) spectroscopy on a Bruker Avance 400 MHz spectrometer operating at resonance frequencies of 104.2 and 79.4 MHz, respectively.

The nitrogen physisorption analysis of the catalysts was measured on a Beckman Coulter SA 3100 in which the catalysts were outgassed at 573 K for 1 h prior to the analysis. Then, adsorption of nitrogen was carried out at 77 K. The textural properties (surface area, pore size distribution, and pore volume) were determined from the sorption isotherms using a non-local density functional theory (NLDFT) method.

FTIR spectra of the fresh catalysts were acquired on Agilent Cary 640 FTIR Spectrometer using the KBr method with a scan range of 400–4000 $cm^{-1}$. The basicity of the catalysts was determined by using pyrrole acid probe molecule. For measurement of IR spectra, a self-supported wafer placed in a high-temperature stainless steel cell with $CaF_2$ windows was activated at 673 K for 1 h. Then, the activated catalyst was exposed to 4 Torr of pyrrole at room temperature for 5 min, followed by outgassing at room temperature. All spectra were recorded at room temperature.

A JEOL JES-FA100 ESR spectrometer was used to observe the formation of unpaired electrons in oxygen vacancies after in vacuo heating. The sample was activated at 673 K for 1 h followed by flowing under $H_2$ stream (10 ml/min) at 673 K for 1 h. All signals were recorded at room temperature.

The X-ray photoelectron spectroscopy (XPS) measurements were conducted on a Shimadzu Axis Ultra DLD spectrometer equipped with an Al Kα radiation source. XPS data were analyzed using CasaXPS software.

Prior to the CO adsorbed FTIR study, the sample was activated at 673 K for 1 h followed by flowing under $H_2$ stream (10 ml/min) at 673 K for 1 h. After that, the activated catalyst was exposed to 20 Torr of CO at room temperature, followed by adsorbing at room temperature, 323, 373, 423, 473, 523, 573, and 623 K.

For CO and $H_2$ adsorbed FTIR study, the activated catalyst was exposed to 20 Torr of CO and 160 Torr of $H_2$ at room temperature, followed by adsorbing at room temperature, 323, 373, 423, 473, 523, 573, and 623 K. For CO and $H_2$ adsorbed ESR study, the sample was activated using the same procedure as above. Then, the activated catalyst was exposed to 20 Torr of CO and 160 Torr of $H_2$ at room temperature, followed by stepwise heating from 323 to 473 K in 50 K increments.

Coke deposits on the catalysts were characterized with a PerkinElmer Thermogravimetric Analyzer 6. The temperature of the furnace was set within the range of 303–973 K with an increment of 293 K/min.

### 2.3. Catalytic performance

Carbon monoxide methanation was carried out in a fixed-bed quartz reactor at a temperature range of 423–723 K. Prior to the reaction, 0.2 g of catalyst was subjected to oxygen treatment at 773 K for 1 h, followed by hydrogen reduction at 773 K for 3 h. Then, the reactor was cooling down to the desired reaction temperature in the presence of hydrogen stream. When the temperature became stable, a mixture of $H_2$ and CO was passed over the activated catalyst at a specific gas hourly space velocity (GHSV) of 13,500 ml $g^{-1}$ $h^{-1}$ and the $H_2$/CO mass ratio of 8/1. The composition of the products was analyzed by an on-line 6090 N Agilent gas chromatograph equipped with a TCD detector. The moisture trap was installed at the outlet gas line of the reactor to prevent moisture from entering the GC. The CO conversion, $CH_4$ formation, rate of CO
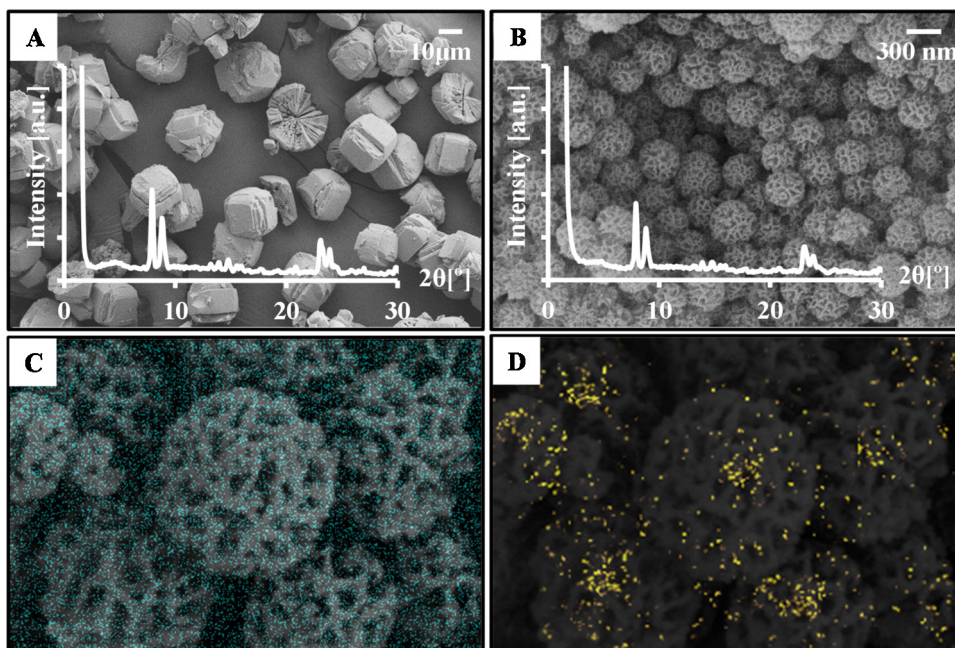
**Fig. 1.** FESEM images and XRD patterns of (A) RmZSM-5, (B) FmZSM-5, and (C) elemental mapping Si, and (D) elemental mapping Al of FmZSM-5.

conversion and rate of $CH_4$ formation were calculated according to the following equations:

$$CO\ conversion(\%) = \frac{M_{CH_4} + M_{CO_2}}{M_{CO} + M_{CH_4} + M_{CO_2}} \times 100 \tag{1}$$

$$CH_4\ selectivity\ (\%) = \frac{M_{CH_4}}{M_{CH_4} + M_{CO_2}} \times 100 \tag{2}$$

$$CH_4 formation(\%) = \frac{M_{CH_4}}{M_{CO} + M_{CH_4} + M_{CO_2}} \times 100 \tag{3}$$

$$CO_2 formation(\%) = \frac{M_{CO_2}}{M_{CO} + M_{CH_4} + M_{CO_2}} \times 100 \tag{4}$$

$$Rate\ of\ CO\ conversion = \frac{n_{CO}}{SA \times W_{cat} \times s} \tag{5}$$

$$Rate\ of\ CH_4 formation = \frac{n_{CH_4}}{SA \times W_{cat} \times s} \tag{6}$$

where, $M_{CO}$, $M_{CH_4}$, and $M_{CO_2}$ is the mole of the CO, $CH_4$, and $CO_2$, respectively. The rate of CO conversion or $CH_4$ formation is reported as moles of CO converted ($n_{CO}$) or $CH_4$ produced ($n_{CH_4}$) divided by the surface area of the catalyst (SA), weight of the catalyst for the reaction ($W_{cat}$) and time (s). The value of the oxygen vacancy is the total intensity of the peak signals at g = 1.99 and g = 1.91 obtained from ESR analysis after outgassing at 673 K. On the other hand, the value of the basicity is the intensity of the peak at 3478 cm$^{-1}$ obtained from FTIR adsorbed pyrrole analysis at room temperature, followed by heating in vacuum at room temperature.

## 3. Results and discussion

### 3.1. Physical properties of the catalysts

Fig. 1 demonstrates FESEM images and elemental mapping analysis of RmZSM-5 and FmZSM-5. RmZSM-5 showed typical coffin-morphology of MFI zeolite catalyst (Fig. 1A). While, FmZSM-5 showed spherical well-ordered dendrimeric morphology with uniform size of 350–400 nm (Fig. 1B). Elemental mapping analysis of FmZSM-5 showed a well dispersed Si atoms (Fig. 1C) and intensely focused Al atoms (Fig. 1D) in the center of each sphere. We suggested that the center of the sphere was probably consist of
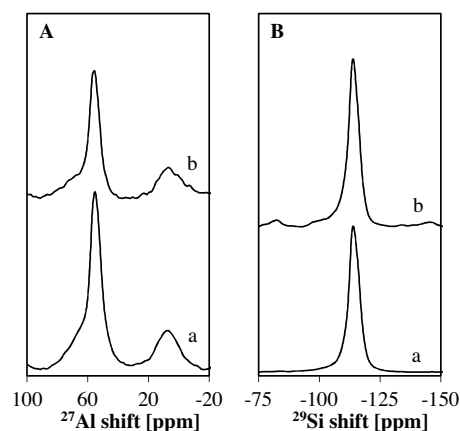


**Fig. 2.** (A) $^{27}$Al MAS NMR and (B) $^{29}$Si MAS NMR spectra of (a) RmZSM-5 and (b) FmZSM-5.

an aluminosilicate framework of ZSM-5, while the dendrimer was fully composed with silica. This result may claimed the formation of a core–shell structure of FmZSM-5.

XRD patterns of RmZSM-5 and FmZSM-5 catalysts are shown in Fig. 1. Both catalysts exhibited diffraction peaks in the range of 2θ = 7–10° and 22–25°, which were identified as reflections for the MFI-type zeolite [13]. No significant changes were observed. However, the peak intensity of FmZSM-5 was slightly lower as compared to the RmZSM-5. This may be due to the addition of silica species during the formation of dendrimeric silica fiber. The well-resolved and rather intense peaks evidenced the highly crystalline structure of FmZSM-5.

Fig. 2 shows $^{27}$Al MAS NMR and $^{29}$Si MAS NMR spectra of catalysts. Two distinct signals of $^{27}$Al MAS NMR spectra at 56 ppm and around 0 ppm, were assigned to tetrahedral aluminium and octahedral aluminium, respectively [14]. The decrease of both signals in FmZSM-5 may be due to the presence of partial dealumination and the occurrence of the crystallization process. On the other hand, $^{29}$Si MAS NMR spectra of RmZSM-5 and FmZSM-5 exhibited one main signal (at −114 ppm) typically observed for (≡SiO)$_4$Si species,
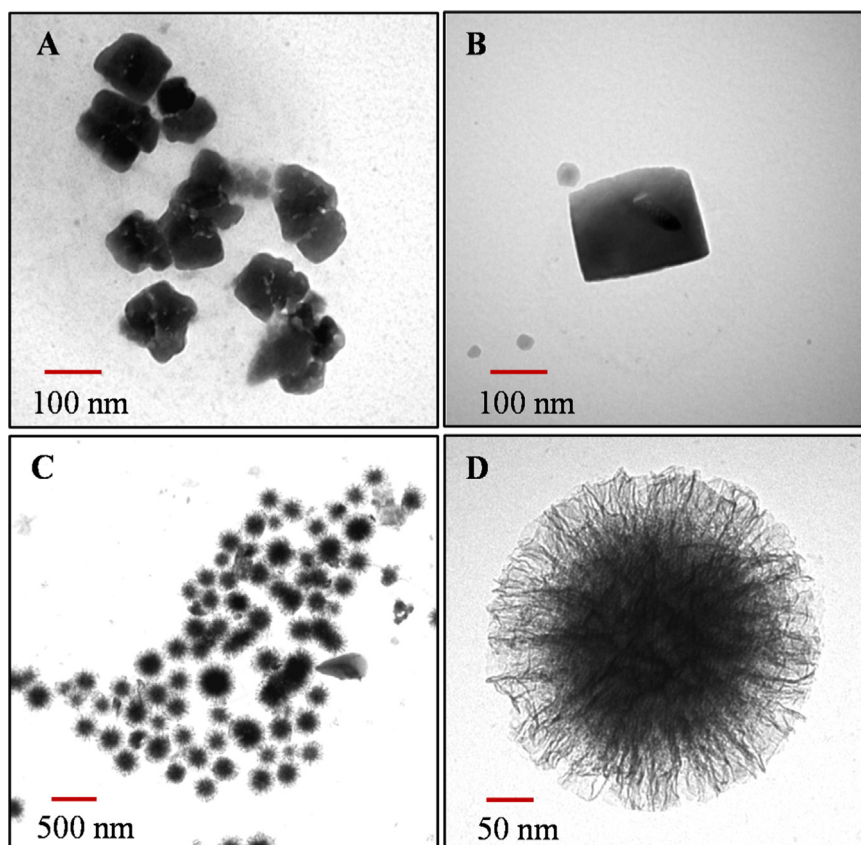
**Fig. 3.** TEM images of (A) RmZSM-5, (B) closed up single particle of RmZSM-5, (C) FmZSM-5, and (D) closed up a single particle of FmZSM-5.

evidencing the highly structured framework and high crystallinity of the ZSM-5 zeolite [15]. Additionally, a weak shoulder signal at $-100$ ppm was observed, which assigned for $(\equiv SiO)_3Si$ species. In fact, an increase in the signal of $(\equiv SiO)_4Si$ species may support the elemental mapping analysis and XRD result of the formation of core-shell structure in FmZSM-5.

Fig. 3 shows TEM images of RmZSM-5 and FmZSM-5. TEM images of the RmZSM-5 clearly depicted their coffin-shaped particle with cluster of some irregular particles (Fig. 3A and B). On the contrary, spherical FmZSM-5 showed fibrous dendrimeric particles (Fig. 3C and D). From closed up single particle image of FmZSM-5 in Fig. 3D, it showed the dendrimers covering the core is densely located with a small distance between the dendrimers.

Fig. 4 illustrates the nitrogen adsorption-desorption isotherms and NLDFT pore size distribution of catalysts. Both catalysts demonstrated type IV isotherm with type H1 hysteresis loop, which typically presents in mesoporous materials [16,17]. The nitrogen uptake at lower $P/P_0$ are attributed to the microporous nature of the catalysts [18]. In addition, the nitrogen uptake at $P/P_0 = 0.2$ and 0.9 are assigned to intra- and interparticle pores, respectively [19]. It is noteworthy that a huge difference was observed in $P/P_0 = 0.9$ of FmZSM-5 with respect to the RmZSM-5. This result revealed that the presence of the fibrous dendrimeric morphology contributed to the large amount of interparticle pores.

The pore size distributions are derived from NLDFT method. RmZSM-5 had pore size distribution in the range of 2–9 nm. On the other hand, FmZSM-5 exhibited main pore size distributions in the range of 2–10 nm and the large pore ranging from 10 to 26 nm. The former is corresponded to the mesopores from self-assembly of CTAB surfactant and the latter is corresponded to the radially orientated mesopores or also known as inter-dendrimer distances that may contribute to the increase in the interparticle
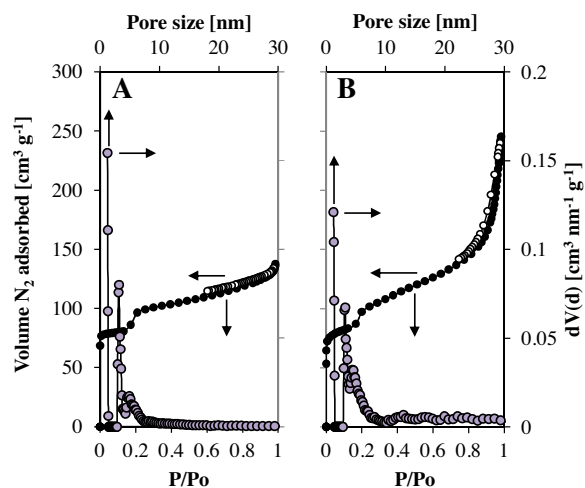


**Fig. 4.** Nitrogen adsorption-desorption isotherms and NLDFT pore size distribution of (A) RmZSM-5 and (B) FmZSM-5.

porosity at high relative pressure ($P/P_0 = 0.9$) [20,21]. In terms of surface area, RmZSM-5 presented a larger surface area ($529\,m^2\,g^{-1}$) as compared to the FmZSM-5 ($479\,m^2\,g^{-1}$). Besides, the total pore volume was $0.201\,cm^3\,g^{-1}$ for the RmZSM-5, significantly altered from the result of FmZSM-5 which is $0.351\,cm^3\,g^{-1}$. Interestingly, this indicated the formation of FmZSM-5 with enormous amount of pores. Despite the lower surface area of FmZSM-5, the fibrous pore network of FmZSM-5 may lead to the highly accessible pores or "exposed" catalytic active sites for adsorption of CO and $H_2$. This result showed that porosity plays an undoubtedly major role in the material.
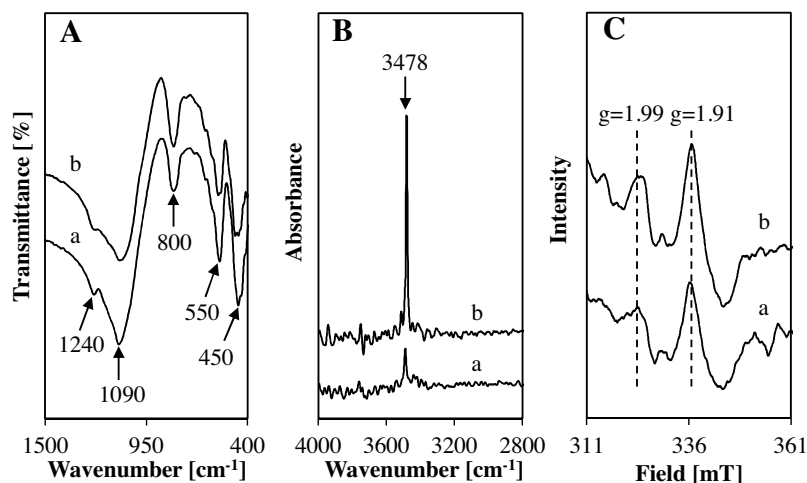
**Fig. 5.** (A) FTIR spectra of fresh catalysts and (B) FTIR spectra of pyrrole adsorbed on activated catalysts at room temperature, followed by heating in vacuum at room temperature, and (C) ESR signals after outgassing at 673 K of (a) RmZSM-5 and (b) FmZSM-5.

FTIR spectroscopy is a very useful technique for obtaining vibrational information about the species in the materials. Fig. 5A shows the FTIR spectra of RmZSM-5 and FmZSM-5 in the region between 1500 and 400 cm$^{-1}$. Typical absorbance bands due to ZSM-5 zeolite were observed for RmZSM-5 and FmZSM-5. The bands at 1240 and 1090 cm$^{-1}$ are assigned to the asymmetric stretching vibrations of Si-O-Si in the framework, while, the band at 800 cm$^{-1}$ is attributed to symmetric stretching vibrations of Si-O-Si in the framework [22]. Another band at 550 cm$^{-1}$ is corresponded to the double five-membered rings of the MFI-type ZSM-5 structure [23]. A band at 450 cm$^{-1}$ is associated to Si-O-Si bending in the framework [24]. These bands represented a typical adsorption bands for MFI type zeolite.

In the present work, basic property of the catalyst is studied as it is important for catalytic performance of CO methanation. The FTIR spectra of adsorbed pyrrole were obtained to quantitatively measure the basic sites of the catalyst. Fig. 5B represents the FTIR spectra of pyrrole adsorption on the catalysts. A sharp peak was observed at 3478 cm$^{-1}$ which can be assigned to perturbed N—H stretch of pyrrole molecules interacting with the basic sites of the framework oxygen atoms. The H-donor properties of pyrrole allowed the formation of $C_4H_4NH$—O bridges with basic oxygen [25,26]. It is noteworthy that FmZSM-5 showed greatly enhanced basic sites with respect to RmZSM-5.

The basicity has a close relationship with the surface defect/oxygen vacancy [27,28]. When an oxygen vacancy is created, two unpaired electrons are left behind, which pulls in the catalyst a very strong Lewis base. The more vacancies are created, the stronger the Lewis basicity of the surface. Theoretically, it is possible that an increase in basicity (which is an increment in the ability of the surface to donate electrons) will increase the reactivity of the catalyst [29].

In addition, ESR spectroscopy has been applied to study the materials with unpaired electrons. This technique is used to detect the occurrence of oxygen vacancies. Fig. 5C shows ESR signals of the catalysts after outgassing at 673 K. The signal appearing at g = 1.99 signifies trapped electrons or unpaired electrons that have localized in oxygen vacancies. Besides, the signal at g = 1.91 is ascribed to the paramagnetic oxygen vacancies [30]. It should be noted that FmZSM-5 possessed a higher amount of oxygen vacancies in surface defect with regard to RmZSM-5. This may be due to the development of dendrimeric morphology, led to the increase in the oxygen vacancies and further contributed to the increase in basicity of FmZSM-5. In this catalyst system, we may claim that the
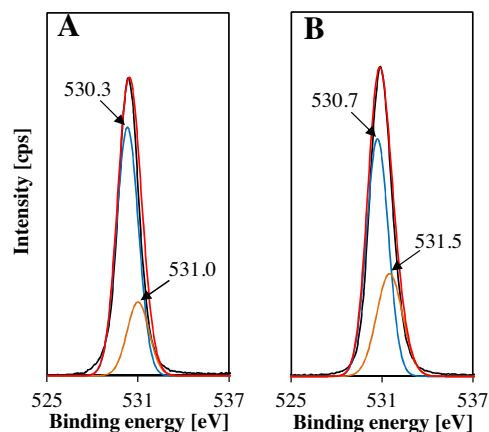


**Fig. 6.** XPS spectra of O 1s of (A) RmZSM-5 and (B) FmZSM-5.

active sites of the catalyst are both basic framework oxygen (zeolite component) and oxygen vacancy (fibrous silica).

X-ray photoelectron spectroscopy (XPS) analysis was carried out to provide information about the nature of the oxygen species. Fig. 6 shows XPS spectra of O 1 s of RmZSM-5 and FmZSM-5. For both catalysts, two types of oxygen species were observed at 530.3–530.7 eV and 531.0–531.5 eV, respectively. The first band is assigned to lattice oxygen. While, the latter is associated with oxygen vacancies or defects [31,32]. The results of ESR and XPS analyses confirmed the existence of oxygen vacancy surface defect in our samples.

Fig. 7A and B show FTIR spectra of CO adsorption on RmZSM-5 and FmZSM-5. The blank test of CO adsorption (without catalyst) showed two main peaks at 2170 and 2120 cm$^{-1}$, which assigned to the gaseous CO. No other significant peak was observed. With the presence of the catalyst, three peaks were observed. Two peaks at the higher wavenumber were corresponded to gaseous CO. While, a peak at 1900 and 1930 cm$^{-1}$, attributed to the bridged CO species was observed for RmZSM-5 and FmZSM-5, respectively [33]. Fig. 7C shows the Gaussian deconvolution peak area at 1900 (for RmZSM-5) or 1930 cm$^{-1}$ (for FmZSM-5) of bridged CO adsorbed at room temperature and 623 K. It should be noted that the peak area at 1900 cm$^{-1}$ was lower than that of 1930 cm$^{-1}$ for both temperatures, indicating that FmZSM-5 possessed higher adsorbed CO species compared to RmZSM-5.

Fig. 8 shows FTIR spectra of CO and $H_2$ adsorption on RmZSM-5 and FmZSM-5. Analogous to our previous study [34], two bands
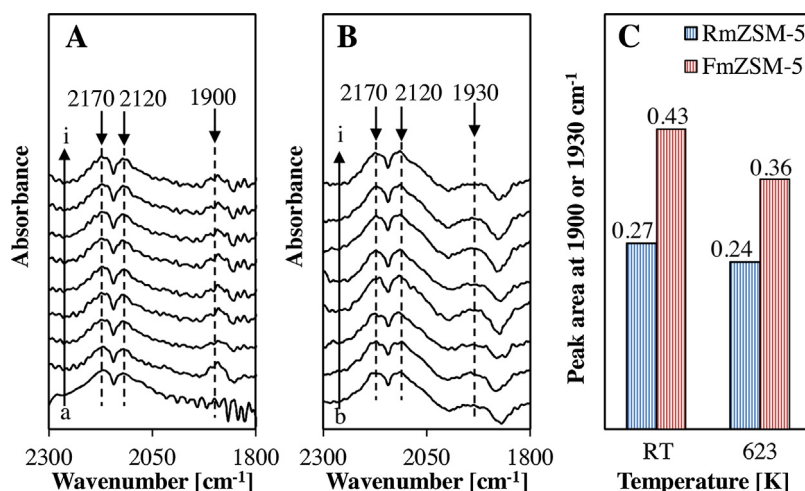
**Fig. 7.** FTIR spectra of adsorbed CO on (A) RmZSM-5 and (B) FmZSM-5. The samples were adsorbed at (b) room temperature, (c) 323 K, (d) 373 K, (e) 423 K, (f) 473 K, (g) 523 K, (h) 573 K, and (i) 623 K. (a) blank test of CO adsorption (without catalyst). (C) Peak area at 1900 (for RmZSM-5) or 1930 cm$^{-1}$ (for FmZSM-5) of adsorbed CO at room temperature (RT) and 623 K, which obtained from Gaussian deconvolution.
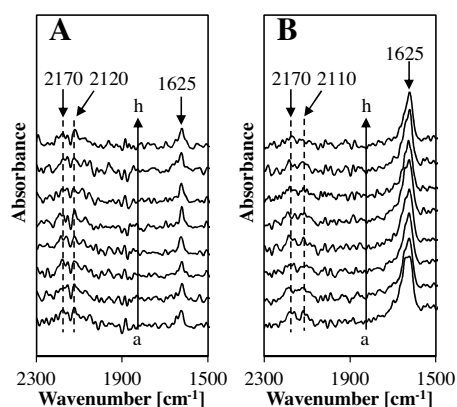


**Fig. 8.** FTIR spectra of adsorbed gases CO and H$_2$ on (A) RmZSM-5 and (B) FmZSM-5. The samples were adsorbed at (a) room temperature, (b) 323 K, (c) 373 K, (d) 423 K, (e) 473 K, (f) 523 K, (g) 573 K, and (h) 623 K.



**Fig. 9.** ESR signals of (A) RmZSM-5 and (B) FmZSM-5 after outgassing at 673 K and heated in the presence of CO and H$_2$ at (a) 323 K, (b) 373 K, (c) 423 K, and (d) 473 K.

were observed at 2170 and 2120 cm$^{-1}$ corresponding to gaseous CO. In addition, a band at 1625 cm$^{-1}$ corresponding to atomic hydrogen. However, it should be noted that the band of atomic hydrogen at 1625 cm$^{-1}$ was remarkably enhanced in FmZSM-5. This may be due to the presence of abundance dendrimers at the outer sphere of the particles that promotes the adsorption of atomic hydrogen. It should be noted that the abundance of atomic hydrogen supply is essential for hydrogenate of CO to form methane.

In the present work, ESR spectroscopy was also used to observe the interaction of CO and molecular hydrogen with RmZSM-5 and FmZSM-5. Fig. 9 shows the ESR signals of CO and H$_2$ adsorption for RmZSM-5 and FmZSM-5. The introduction of CO and H$_2$, followed by heating, resulted in the formation of electrons where the electrons were stabilized in these oxygen vacancies, resulting in the reduction of the ESR signal at g = 1.99. Besides, the observed signal at g = 1.91 is associated with the paramagnetic oxygen vacancies present in the sample was simultaneously decreased [30]. The decrease in the intensity of these two signals probably due to the adsorption of CO and H$_2$ on these oxygen vacancies. This phenomenon indicated that some of the oxygen vacancies were filled with electrons, which may have originated from gaseous CO and/or atomic hydrogen. The presence of these oxygen vacancies not only promoted the adsorption capacity of the CO and H$_2$, but also improved their dissociation properties due to allocation of
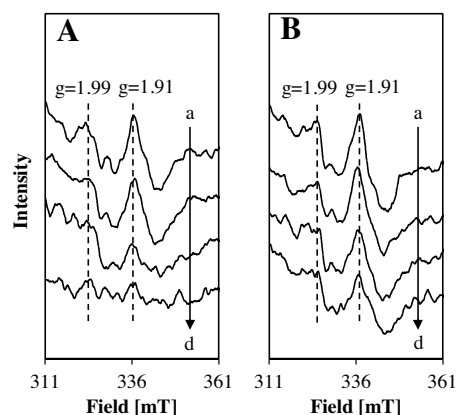
electron into these oxygen vacancies [35]. As the results, the presence of oxygen vacancies in surface defect may provide another platform for CO and H$_2$ adsorption.

### 3.2. Catalytic performance

Figs. 10 and 11A,B, show the catalytic performance of RmZSM-5 and FmZSM-5 for CO methanation in the temperature range of 400–800 K. FmZSM-5 showed superior catalytic activity than that of RmZSM-5. The catalytic activity appeared very low at and below 700 K, but increased at 723 K may be due to the increase in the methanation reaction accompanied by the water-gas shift (WGS) reaction [36]. In this study, the catalytic performance of both catalysts almost same at the low temperature region (423–673 K), but significantly improved at 723 K may be due to the system's energy starts to be high enough for both CO and H$_2$ to dissociate and interact to form methane [37]. At 723 K, FmZSM-5 showed 63% of CO conversion, 69% of CH$_4$ selectivity, and 44% of CH$_4$ formation. On the other hand, RmZSM-5 displayed 42% of CO conversion and 80% of CH$_4$ selectivity, and 34% of CH$_4$ formation. The lower CH$_4$ selectivity for FmZSM-5 than that for RmZSM-5 may be due to the happening of water-gas shift (WGS) side reaction. This side reaction has led to the formation of CO$_2$. As shown in Fig. 10, CO$_2$ formation showed an increasing trend with increasing in temperature. Hence, we can conclude that CO$_2$ did not convert to CH$_4$ in
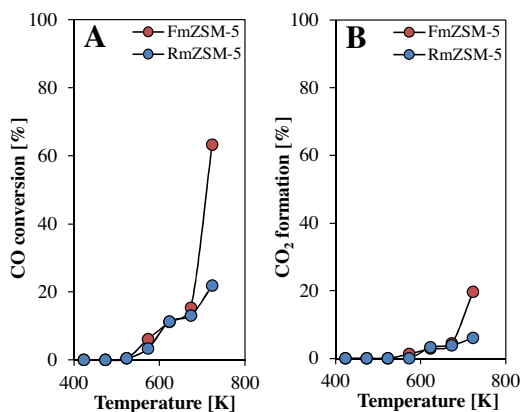
Fig. 10. (A) CO conversion, (B) $CO_2$ formation as a function of the reaction temperature at GHSV = 13,500 ml g$^{-1}$ h$^{-1}$ and $H_2$/CO = 8/1 over RmZSM-5 and FmZSM-5.



Fig. 12. (A) DTG and (B) TGA curves of fresh RmZSM-5 (RmZSM-5-F), spent RmZSM-5 (RmZSM-5-S), fresh FmZSM-5 (FmZSM-5-F), and spent FmZSM-5 (FmZSM-5-S).

the current study. In term of reaction rate, the rate of CO conversion and $CH_4$ formation of RmZSM-5 were 0.0367 μmol-CO/m$^2$ s and 0.0296 μmol-$CH_4$/m$^2$ s, respectively. While, a higher rate of CO conversion and $CH_4$ formation of 0.0708 μmol-CO/m$^2$ s and 0.0488 μmol-$CH_4$/m$^2$ s, respectively, were observed for FmZSM-5. The catalytic results showed that FmZSM-5 performed remarkably with enhanced catalytic activity over RmZSM-5 in CO methanation. Besides, only a small amount of $CO_2$ and $H_2O$ by-product were formed. No other by-products were detected. Moreover, the catalytic activity of FmZSM-5 was sustained for 50 h of the reaction at 723 K under atmospheric pressure, which manifested that it is very stable under the applied reaction conditions.

The apparent activation energies ($E_a$) for CO methanation over RmZSM-5 and FmZSM-5 were determined by using the Arrhenius equation in the range of 673–723 K. The $E_a$ values of RmZSM-5 and FmZSM-5 are found to be 106 and 104 kJ mol$^{-1}$, which is in good agreement with the previous literatures though the activation energy might vary considerably with the nature of the support and the catalytic reaction conditions. Comparable values for the $E_a$ were reported by Liu et al. for Ni-$V_2O_3$/$Al_2O_3$ catalysts (86–109 kJ mol$^{-1}$) [38] and Li et al. for Ni/$CeO_2$-$Al_2O_3$/Ni-foam catalyst (~151 kJ mol$^{-1}$) [39].

Fig. 11C shows the dependence of catalytic activity on the oxygen vacancy and basicity. The result showed a good correlation between oxygen vacancy and the rate of $CH_4$ formation in CO methanation at 723 K. On the contrary, there is less correlation
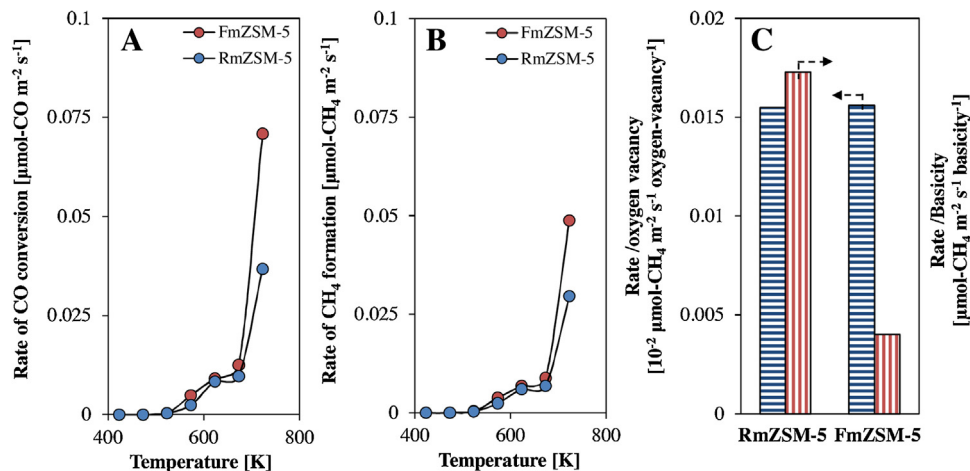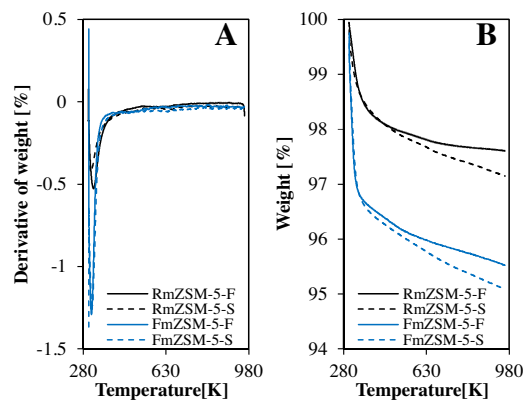
found between the basicity and the rate of $CH_4$ formation. The ratio of the rate of $CH_4$ formation to oxygen vacancy did not change much for RmZSM-5 and FmZSM-5, indicating that the catalytic activity is clearly correlated with the oxygen vacancy. While, no dependence of activity on the basicity was observed. This result revealed that the methanation activity is more governed by oxygen vacancy.

Previous reports have been investigated on the relationship between oxygen vacancy and catalytic performance. Song et al. reported a linear dependence between the hydrogenation activity and oxygen vacancy concentration in oxygen-deficient tungsten oxide catalysts [40]. Moreover, Zhou et al. reported the surface oxygen vacancy-dependent electrocatalytic activity of tungsten oxide nanowires, in which these surface oxygen vacancy served as catalytic site descriptors [41]. In addition, Zhang et al. studied the relation of surface defects (surface oxygen vacancies or defects) with the photocatalytic activity [42]. The result showed that surface defects gave a positive effect on the photocatalytic activity. However, they could not show a relationship of the photocatalytic activity with the surface defects as the x-ray photoelectron and photoluminescence spectroscopy are not suitable for quantitative analysis.

The presence of coke deposition is known to cause catalyst deactivation. Therefore, in this study, coke deposition on the catalysts were examined by TG-DTG analysis. Fig. 12 shows TG-DTG analysis of fresh and spent catalysts. From the results, only a negligible amount of coke was observed on both RmZSM-5 and FmZSM-5 and the highest coke content was only ~0.5%. To summarize, FmZSM-



Fig. 11. (A) Rate of CO conversion, (B) rate of $CH_4$ formation as a function of the reaction temperature at GHSV = 13,500 ml g$^{-1}$ h$^{-1}$ and $H_2$/CO = 8/1, and (C) oxygen vacancy and basicity dependences of the rate of $CH_4$ formation at 723 K over RmZSM-5 and FmZSM-5.

**Table 1**
Physicochemical properties of the catalysts.

| Catalysts | XRD crystallinity[a] (%) | Surface area[b] ($m^2 g^{-1}$) | Average pore size[b] (nm) | Total pore volume[b] ($cm^3 g^{-1}$) | Mesopore volume[c] ($cm^3 g^{-1}$) | $B_{sample}/B_F$[d] (a.u.) | $OV_{sample}/OV_F$[e] (a.u.) | Apparent activation energy, $E_a$[f] (kJ $mol^{-1}$) | Weisz–Prater value[g] $\times 10^{-4}$ |
|---|---|---|---|---|---|---|---|---|---|
| RmZSM-5 | 64 | 529 | 2.59 | 0.201 | 0.187 | 0.1406 | 0.6099 | 106 | 4.37 |
| FmZSM-5 | 52 | 479 | 4.50 | 0.351 | 0.337 | 1 | 1 | 104 | 4.24 |

[a] The calibration curve of crystallinity was used to determine the crystallinity of the catalyst. It was plotted against average peak intensity at $2\theta = 7.8°$ and $8.9°$ of the catalyst, in which $SiO_2$ and mZSM-5 was assumed to be 0 and 100% crystallinity, respectively. Crystallinity of the catalyst was calculated from linear equation obtained from the calibration curves.

[b] Determined from non-local density functional theory (NLDFT) method.

[c] Mesopore volume was obtained using total pore volume − micropore volume which was obtained from $t$-plot method.

[d] Ratio of basicity, $B_{sample}/B_F$ was obtained by the peak intensity of sample/peak intensity of FmZSM-5, in which sample = RmZSM-5 and FmZSM-5. The peak intensity at 3478 cm was acquired from FTIR of pyrrole adsorption.

[e] Ratio of oxygen vacancy, $OV_{sample}/OV_F$ was obtained by the peak intensity of sample/peak intensity of FmZSM-5, in which sample = RmZSM-5 and FmZSM-5. The peak intensity is the total intensity of the peak signals at g = 1.99 and g = 1.91 obtained from ESR analysis.

[f] $E_a$ values were determined in the range of 673–723 K.

[g] Determined from Weisz–Prater criterion under reaction conditions: P = 1 atm and T = 723 K.

5 catalyst is resistant toward coke formation and possessed high stability for the methanation reaction up to 50 h of time on stream.

These results showed the importance of support morphology on the catalytic performance of CO methanation. Apparently, the presence of oxygen vacancies led to the high interparticle porosity, high basicity and even more importantly, high CO and $H_2$ adsorption sites in FmZSM-5 should be responsible for the enhancement in the catalytic activity and high stability in CO methanation. The role of support morphology in this study is also supported by Gao et al. who reported that the morphology of $CeO_2$ strongly affected the reduction behavior, oxygen vacancies and hydroxyl reactivity of the catalyst [43].

It is well known that oxygen vacancies in surface defect strongly influenced the physicochemical properties of the catalyst. These oxygen vacancies play a significant role for adsorption of molecules in heterogeneous catalysis [44]. Liu et al. investigated the enhanced CO methanation over a Ni-$V_2O_3$/$Al_2O_3$ catalyst [38]. In this case, oxidation-reduction properties of $V_2O_3$ promoter plays a role for CO dissociation and increased the oxygen vacancies. These oxygen vacancies act as the active site for $CO_2$ by-product dissociation and further generated surface oxygen intermediate, thus preventing carbon deposition and improve the high-temperature stability of the catalyst. In addition, Nematollahi et al. reported that lattice deformation (entrance of $Ni^{2+}$ cations into $CeO_2$ lattice and replaces some $Ce^{4+}$ ions) and charge imbalance (changing oxidation between $Ce^{3+}$ and $Ce^{4+}$) at the ceria structure led to the formation of oxygen vacancies. Indirectly, the presence of these oxygen vacancies can promote CO methanation over a Ni/$CeO_2$ catalyst by making easier migration of free electrons from support to the interface of metal-support, then, leading to weakening of the CO bond by electron back donation effect [45]. The importance role of oxygen vacancies in zirconia-based catalysts have been previously reported in the literatures. Pan et al. reported the preparation of Ni/$Ce_{0.5}Zr_{0.5}O_2$ by an impregnation method for $CO_2$ methanation and one of the reasons that explained the high activity of the catalyst was due to the presence of higher oxygen vacancies as compared to other preparation methods [46]. Besides, Takano et al. reported the presence of tetragonal $ZrO_2$ with enriched oxygen vacancies by the introduction of $Ni^{2+}$ and $Ca^{2+}$ may possibly contribute to the high catalytic activity of $CO_2$ methanation [47]. Furthermore, Ren et al. studied the effect of second metals (Fe, Co, and Cu) in Ni/$ZrO_2$ for $CO_2$ methanation [48]. The results showed that Fe assisted in the reduction of $ZrO_2$ support and further induce the formation of more oxygen vacancies, which have an important role in promoting adsorption and dissociation of $H_2$ and $CO_2$, thus enhancing the $CO_2$ methanation activity.

The accessibility of the active sites and so the diffusion limitations are also significant factors in determining the catalytic activity of the catalyst. The Mears' criterion is used to determine the effect of the external diffusion limitation [49]. In this case, we assumed that the mass transfer in the surface around the particles was a fast step, therefore, the reaction was not limited by the external diffusion limitation. In addition, the Weisz–Prater criterion is used as the estimation for internal diffusion limitation which takes the catalyst porosity into account. To evaluate if the internal diffusion limitation affected the overall CO methanation rate under our reaction conditions, the Weisz–Prater criterion was applied as equation given below and the internal diffusion limitation can be neglected if [50–52]:

$$N_{WP} = \frac{\Re R_P^2}{C_S D_{eff}} < 1 \tag{7}$$

where $\Re$ = reaction rate of CO per volume of catalyst (mol/$cm^3$ s).

$R_p$ = catalyst particle radius (cm).

$C_s$ = reactant concentration at the external surface of the catalyst (mol/$cm^3$).

$D_{eff}$ = effective pore diffusivity ($cm^2$/s).

Under the studied reaction conditions (P = 1 atm and T = 723 K), the value of Weisz-Prater criterion for RmZSM-5 and FmZSM-5 were $4.37 \times 10^{-4}$ and $4.24 \times 10^{-4}$, respectively. The calculation of Weisz–Prater criterion indicated absence of internal mass transfer limitations in this system with the observed reaction rates. It is worth mentioning that internal mass transfer in RmZSM-5 is slightly higher as compared to FmZSM-5. Herein, we may conclude that the presence of fibrous morphology may contribute to the improved in the accessibility of the active sites. The physicochemical properties of the catalysts are summarized in Table 1.

Regrettably, there is almost no report about the application of fibrous silica mesoporous ZSM-5 for CO methanation. However, based on previous literatures, fibrous materials have been applied in other catalytic testing due to its excellent properties. Recently, our research group have studied on the use of fibrous silica ZSM-5 for cumene hydrocracking [53]. Besides, a new family of high-surface area silica nanospheres (KCC-1) with fibrous morphologies was first discovered by Polshettiwar et al. [54]. This material possesses a good potential for silica-supported catalysts, as it possessed high surface area, good thermal and hydrothermal stabilities, high mechanical stability, and high accessibility of active sites. In recent study, Fihri et al. reported the application of fibrous nano-silica supported ruthenium (KCC-1/Ru) in hydrogenolysis of alkanes [55]. The results showed that high catalytic activity was due to the highly accessible KCC-1 support while excellent stability was probably due to the fibrous nature of the support. Additionally,

Bouhrara et al. studied the use of nitridated fibrous silica (KCC-1) for Knoevenagel condensations and transesterification reactions [56]. The high reaction activity was due to the fibrous morphology with the highly accessibility of basic and acidic sites. Contemporaneously, Peng et al. reported a center radially fibrous silica encapsulated TS-1 zeolite (TS-1@KCC-1) with enhanced hydrothermal and mechanical stability for one-pot synthesis of benzamide [57]. Moreover, Dong et al. prepared fibrous nano-silica (KCC-1) with dandelion-like shape, high surface area, and easy accessibility of active sites to immobilize of Ni@Pd nanoparticles for the reduction of 4-nitrophenol and hydrodechlorination of 4-chlorophenol [58].

## 4. Conclusion

A core-shell fibrous silica mesoporous ZSM-5 (FmZSM-5) was prepared by using microemulsion system coupled with zeolite crystal-seed crystallization method for the methanation of CO. It should be noted that the presence of oxygen vacancies increased the interparticle porosity, basicity, and CO and $H_2$ adsorption sites in FmZSM-5. These properties can be explained as the factors that contributed to the high catalytic activity and stability of FmZSM-5 in CO methanation with rate of CO conversion and $CH_4$ formation of 0.0708 $\mu$mol-CO/m$^2$ s and 0.0488 $\mu$mol-CH$_4$/m$^2$ s at 723 K. As well, the accessibility of active sites showed no diffusion limitation. The development of core-shell fibrous silica mesoporous ZSM-5 is a new breakthrough and potentially important for applications of mesoporous zeolites in the future catalysis applications.

## Acknowledgments

## References

[1] S. Rönsch, J. Schneide, S. Matthischke, M. Schlüter, M. Götz, J. Lefebvre, P. Prabhakaran, S. Bajohr, Fuel 166 (2016) 276–296.
[2] K. Furman, D. Baudouin, T. Margossian, K.D. Sabnis, Y. Cui, F.H. Ribeiro, C. Copéret, J. Catal. 324 (2015) 9–13.
[3] M.A. Lucchini, A. Testino, A. Kambolis, C. Proff, C. Ludwig, Appl. Catal. B Environ. 182 (2016) 94–101.
[4] M.A.A. Aziz, A.A. Jalil, S. Triwahyono, A. Ahmad, Green Chem. 17 (2015) 2647–2663.
[5] X. Dai, J. Liang, D. Ma, X. Zhang, H. Zhao, B. Zhao, Z. Guo, F. Kleitz, S. Qiao, Appl. Catal. B Environ. 165 (2015) 752–762.
[6] A.M. Abdel-Mageed, S. Eckle, R.J. Behm, J. Am. Chem. Soc. 137 (2015) 8672–8675.
[7] J.H. Schulman, W. Stoeckenius, L.M. Prince, J. Phys. Chem. 63 (10) (1959) 1677–1680.
[8] M.A. Malik, M.Y. Wani, M.A. Hashim, Arabian J. Chem. 5 (2012) 397–417.
[9] K. Egeblad, C.H. Christensen, M. Kustova, C.H. Christensen, Chem. Mater. 20 (2008) 946–960.
[10] J.-C. Lin, M.Z. Yates, Langmuir 21 (2005) 2117–2120.
[11] S. Lee, D.F. Shantz, Chem. Mater. 17 (2005) 409–417.
[12] L.P. Teh, S. Triwahyono, A.A. Jalil, R.R. Mukti, M.A.A. Aziz, T. Shishido, Chem. Eng. J. 270 (2015) 196–204.
[13] M.M.J. Treacy, J.B. Higgins, Collection of Simulated XRD Powder Patterns for Zeolites, fourth ed., Elsevier, New York, 2001.
[14] J. Klinowski, Colloids Surf. 36 (1989) 133–154.
[15] P. Bai, P. Wu, W. Xing, D. Liu, L. Zhao, Y. Wang, B. Xu, Z. Yan, X.S. Zhao, J. Mater. Chem. A 3 (2015) 18586–18597.
[16] U. Patil, A. Fihri, A.H. Emwas, V. Polshettiwar, Chem. Sci. 3 (2012) 2224–2229.
[17] D. Gao, A. Duan, X. Zhang, K. Chi, Z. Zhao, J. Li, Y. Qin, X. Wang, C. Xua, J. Mater. Chem. A 3 (2015) 16501–16512.
[18] H. Zhang, L. Chu, Q. Xiao, L. Zhu, C. Yang, X. Meng, F.-S. Xiao, J. Mater. Chem. A 1 (2013) 3254–3257.
[19] S. Kelkar, C.M. Saffron, Z. Li, S.-S. Kim, T.J. Pinnavaia, D.J. Miller, R. Kriegel, Green Chem. 16 (2014) 803–812.
[20] D.-S. Moon, J.-K. Lee, Langmuir 28 (2012) 12341–12347.
[21] Y.-J. Yu, J.-L. Xing, J.-L. Pang, S.-H. Jiang, K.-F. Lam, T.-Q. Yang, Q.-S. Xue, K. Zhang, P. Wu, ACS Appl. Mater. Interfaces 6 (2014) 22655–22665.
[22] Z.N. Siddiqui, K. Khan, N. Ahmed, Catal. Lett. 144 (2014) 623–632.
[23] W. Li, G. Li, C. Jin, X. Liu, J. Wang, J. Mater. Chem. A 3 (2015) 14786–14793.
[24] R. Merkache, I. Fechete, M. Maamache, M. Bernard, P. Turek, K. Al-Dalama, F. Garin, Appl. Catal. A Gen. 504 (2015) 672–681.
[25] H. Forster, H. Fuess, E. Geidel, B. Hunger, H. Jobic, C. Kirschhock, O. Klepel, K. Krause, Phys. Chem. Chem. Phys. 1 (1999) 593–603.
[26] M.A.A. Aziz, A.A. Jalil, S. Triwahyono, R.R. Mukti, Y.H. Taufiq-Yap, M.R. Sazegar, Appl. Catal. B Environ. 147 (2014) 359–368.
[27] M.J. Climent, A. Corma, S. Iborra, K. Epping, A. Velty, J. Catal. 225 (2004) 316–326.
[28] C. Drouilly, J.-M. Krafft, F. Averseng, H. Lauron-Pernot, D. Bazer-Bachi, C. Chizallet, V. Lecocq, G. Costentin, Appl. Catal. A Gen. 453 (2013) 121–129.
[29] D.C. Upham, A.R. Derk, S. Sharma, H. Metiu, E.W. McFarland, Catal. Sci. Technol. 5 (2015) 1783–1791.
[30] R.S. Ningthoujam, D. Lahiri, V. Sudarsan, H.K. Poswal, S.K. Kulshreshtha, S.M. Sharma, B. Bhushan, M.D. Sastry, Mater. Res. Bull. 42 (2007) 1293–1300.
[31] J.M. López, A.L. Gilbank, T. García, B. Solsona, S. Agouram, L. Torrente-Murciano, Appl. Catal. B Environ. 174–175 (2015) 403–412.
[32] G. Wu, Y. Gao, F. Ma, B. Zheng, L. Liu, H. Sun, W. Wu, Chem. Eng. J. 271 (2015) 14–22.
[33] W. Suëtaka, Surface Infrared and Raman Spectroscopy: Methods and Applications, 3, Springer Science & Business Media, New York, 2013.
[34] L.P. Teh, S. Triwahyono, A.A. Jalil, C.R. Mamat, S.M. Sidik, N.A.A. Fatah, R.R. Mukti, T. Shishido, RSC Adv. 5 (2015) 64651–64660.
[35] J. Barrientos, M. Lualdi, M. Boutonnet, S. Järås, Appl. Catal. A Gen. 486 (2014) 143–149.
[36] J.M. Gatica, X. Chen, S. Zerrad, H. Vidal, A.B. Ali, Catal. Today 180 (2012) 42–50.
[37] T. Bligaard, J.K. Nørskov, S. Dahl, J. Matthiesen, C.H. Christensen, J. Sehested, J. Catal. 224 (2004) 206–217.
[38] Q. Liu, F. Gua, X. Lu, Y. Liu, H. Li, Z. Zhong, G. Xua, F. Su, Appl. Catal. A Gen. 488 (2014) 37–47.
[39] Y. Li, Q. Zhang, R. Chai, G. Zhao, Y. Liu, Y. Lu, ChemCatChem 7 (2015) 1427–1431.
[40] J. Song, Z.-F. Huang, L. Pan, J.-J. Zou, X. Zhang, L. Wang, ACS Catal. 5 (2015) 6594–6599.
[41] H. Zhou, Y. Shi, Q. Dong, J. Lin, A. Wang, T. Ma, J. Phys. Chem. C 118 (2014) 20100–20106.
[42] X. Zhang, J. Qin, Y. Xue, P. Yu, B. Zhang, L. Wang, R. Liu, Sci. Rep. 4 (2014) 4596, http://dx.doi.org/10.1038/srep04596.
[43] Y. Gao, R. Li, S. Chen, L. Luo, T. Cao, W. Huang, Phys. Chem. Chem. Phys. 17 (2015) 31862–31871.
[44] S. Huygh, E.C. Neyts, J. Phys. Chem. C 119 (2015) 4908–4921.
[45] B. Nematollahi, M. Rezaei, E.N. Lay, Int. J. Hydrogen Energy 40 (2015) 8539–8547.
[46] Q. Pan, J. Peng, T. Sun, D. Gao, S. Wang, S. Wang, Fuel Process. Technol. 123 (2014) 166–171.
[47] H. Takano, H. Shinomiya, K. Izumiya, N. Kumagai, H. Habazaki, K. Hashimoto, Int. J. Hydrogen Energy 40 (2015) 8347–8355.
[48] J. Ren, X. Qin, J.-Z. Yang, Z.-F. Qin, H.-L. Guo, J.-Y. Lin, Z. Li, Fuel Process. Technol. 137 (2015) 204–211.
[49] D.E. Mears, J. Catal. 20 (1971) 127–131.
[50] P.B. Weisz, C.D. Prater, Adv. Catal. 6 (1954) 143–196.
[51] S.L. Pirard, C. Diverchy, S. Hermans, M. Devillers, J.-P. Pirard, N. Job, Catal. Comm. 12 (2011) 441–445.
[52] P.M. Mortensen, J.-D. Grunwaldt, P.A. Jensen, A.D. Jensen, Catal. Today 259 (2016) 277–284.
[53] M.L. Firmansyah, A.A. Jalil, S. Triwahyono, H. Hamdan, M.M. Salleh, W.F.W. Ahmad, G.T.M. Kadja, Catal. Sci. Technol. (2016), http://dx.doi.org/10.1039/c6cy00106h.
[54] V. Polshettiwar, D. Cha, X. Zhang, J.M. Basset, Angew. Chem. Int. Ed. 49 (2010) 9652–9656.
[55] A. Fihri, M. Bouhrara, U. Patil, D. Cha, Y. Saih, V. Polshettiwar, ACS Catal. 2 (2012) 1425–1431.
[56] M. Bouhrara, C. Ranga, A. Fihri, R.R. Shaikh, P. Sarawade, A.-H. Emwas, M.N. Hedhili, V. Polshettiwar, ACS Sustain. Chem. Eng. 1 (2013) 1192–1199.
[57] H.-G. Peng, L. Xu, H. Wu, K. Zhang, P. Wu, Chem. Commun. 49 (2013) 2709–2711.
[58] Z. Dong, X. Le, C. Dong, W. Zhang, X. Li, J. Ma, Appl. Catal. B Environ. 162 (2015) 372–380.